ChemEurJ

Research Article
doi.org/10.1002/chem.202501809

Chemistry Europe
European Chemical Societies Publishing

www.chemeurj.org

VIP *Very Important Paper*

Unraveling Structural Evolution of Cobalt-Based Metal-Organic Frameworks for Boosting Nitrate Electroreduction to Ammonia

Zhi Wang,[a, b, c] Yanjun Han,[a, b, c] Depeng Wang,[a, b, c] Daming Zhao,[a, c] Haixia Zhong,*[a, b, c] and Xinbo Zhang*[a, b, c]

Metal-organic frameworks (MOFs) have been widely studied for various complex electrocatalytic reactions, such as nitrate reduction reaction (NO_3RR) to ammonia. Currently, their real active sites are controversial due to the inevitable structure transformations of MOFs during the catalytic process, limiting the rational design of effective electrocatalysts. Here, we clarified the structural evolution of zeolitic imidazole framework-67 (ZIF-67) with Co-N units and Co_3(hexahydroxytriphenylene)$_2$ (Co-HHTP) with Co-O units on carbon paper (CP) toward enhancing NO_3RR. Both ZIF-67/CP and Co-HHTP/CP achieve NH_3 Faradaic efficiencies more than 95% within the wide potential range of -0.2 to -1.0 V versus reversible hydrogen electrode (RHE). At -1.0 V versus RHE, they deliver NH_3 yield rates of 87.41 and 79.11 mg h^{-1} cm^{-2}, respectively, which outperform the most reported MOF-based electrocatalysts. Combining with in-situ Raman and ex-situ X-ray diffraction analysis, we verified the faster transformation of ZIF-67 into $Co(OH)_2$ compared to Co-HHTP. The newly generated $Co(OH)_2$ was recognized as the catalytic species and presented more favorable hydrogenation as elucidated by in-situ Fourier transform infrared and differential electrochemical mass spectroscopy. This work offers insightful understanding on the active phase of MOFs for designing reasonable active units toward different electrochemical reactions.

1. Introduction

Ammonia (NH_3), has been used as an essential industrial chemical for the production of fertilizers, explosives, and plastics, and also shows broad promise in the field of clean energy.[1] For example, NH_3 is regarded as a reliable H_2 carrier and a high-efficiency clean energy owing to its low liquefaction temperature (−33 °C, 0.1 MPa), high hydrogen content (17.6 wt%), considerable volumetric energy density (12.7 MJ L^{-1}, liquid), etc.[2] Currently, NH_3 synthesis relies on the energy-intensive Haber-Bosch process under high temperature and pressure with high carbon emissions.[3] In this context, ambient electrochemical synthesis of NH_3 in aqueous solutions driven by renewable electricity would be one compelling alternative. However, high $N{\equiv}N$ bond energy (941 kJ mol^{-1}) and poor water solubility have seriously limited the NH_3 yield rate under ambient condition using N_2 resource (less than 0.1 mg h^{-1} cm^{-2}).[4,5] Over recent years, electrochemical NO_3^- reduction reaction (NO_3RR) makes it possible to achieve industrial-grade performance because of the low dissociation energy of $N=O$ bond in NO_3^- (204 kJ mol^{-1}) and high solubility.[6,7] Meanwhile, despite the NO_x from the environment, low-temperature air plasma could ensure the sufficient source of NO_3^- toward the large-scale synthesis of green NH_3.[8] Nevertheless, electrochemical conversion of NO_3^- to NH_3 involves eight-electron transfer and multiple reduction pathways, imposing challenges in improving activity and selectivity.[9] Therefore, extensive efforts have been contributed to exploring efficient catalysts for NO_3RR.

Metal-organic frameworks (MOFs) linked by metal ions and organic ligands have shown great potential in electrocatalysis due to their well-defined porous structures and abundant metal sites.[10] For example, two-dimensional (2D) MOF (BIT-119) with asymmetric $Cu\text{-}N_1O_3$ units was precisely constructed to regulate the adsorption strength of key adsorbates in CO_2 reduction reaction (CO_2RR) and achieve a C_2 Faradaic efficiency (FE) of 75%.[11] And the high-density unsaturated Fe sites on 2D Fe-$MOF_{0.3}$ possessed remarkable oxygen evolution reaction (OER, overpotential: 259 mV at 10 mA cm^{-2}) and hydrogen evolution reaction (HER, overpotential: 36 mV at 10 mA cm^{-2}) activity.[12] Besides, cobalt-based MOFs (Co-MOFs) have been reported to exhibit excellent electrochemical performance in NO_3RR. The Ni-BDC@Co-HHTP heterostructure synthesized by Zou et al. delivered an excellent NH_3 yield rate of 11.46 mg h^{-1} cm^{-2} and a high FE of 98.4% at -0.7 V versus reversible hydrogen electrode

---

[a] *Z. Wang, Y. Han, D. Wang, D. Zhao, Prof. H. Zhong, Prof. X. Zhang*
China-Belarus Belt and Road Joint Laboratory on Advanced Materials and Manufacturing, Changchun Institute of Applied Chemistry, Chinese Academy of Sciences, 5625 Renmin Street, Changchun 130022, China
E-mail: hxzhong@ciac.ac.cn
xbzhang@ciac.ac.cn

[b] *Z. Wang, Y. Han, D. Wang, Prof. H. Zhong, Prof. X. Zhang*
School of Applied Chemistry and Engineering, University of Science and Technology of China, 96 Jinzhai Street, Hefei 230026, China

[c] *Z. Wang, Y. Han, D. Wang, D. Zhao, Prof. H. Zhong, Prof. X. Zhang*
State Key Laboratory of Rare Earth Resource Utilization, Changchun Institute of Applied Chemistry, Chinese Academy of Sciences, 5625 Renmin Street, Changchun 130022, China

Supporting information for this article is available on the WWW under https://doi.org/10.1002/chem.202501809

(RHE).[13] Despite the promising catalytic activity of MOF catalysts, the structural stability of MOFs may be open to doubt.[14,15] Generally, reconstructions of MOFs can be driven by the operated conditions (e. g., electrolyte and potential). For instance, the reconstruction of Cu-N_4 single-atom sites into Cu nanoparticles occurred during NO_3RR and then the aggregated nanoparticles were reversibly disintegrated into single atoms under the ambient atmosphere.[16] However, the real active sites of Co-MOF catalysts in NO_3RR remain unclear. Study on the structural evolution of Co-MOFs is crucial to unveil the real active phase and the corresponding structure-activity correlations toward future rational catalyst design.

Herein, we clarified the structural evolution of MOFs during catalytic process using the zeolitic imidazole framework-67 (ZIF-67) with Co-N units and Co_3(hexahydroxytriphenylene)$_2$ (Co-HHTP) with Co-O units on carbon paper (CP). In-situ Raman and ex-situ characterizations (e. g., X-ray diffraction (XRD) and transmission electron microscopy (TEM)) certified the structural transformation of ZIF-67 or Co-HHTP into $Co(OH)_2$. Note that the transformation of Co-HHTP is slower than ZIF-67, requiring a longer time for the complete reconstruction of Co-HHTP into $Co(OH)_2$. Importantly, both ZIF-67/CP and Co-HHTP/CP exhibit NH_3 FEs more than 95% within the wide potential window of −0.2 to −1.0 V versus RHE. And high NH_3 yield rates of 87.41 and 79.11 mg h^{-1} cm^{-2} at −1.0 V versus RHE are separately achieved by ZIF-67/CP and Co-HHTP/CP, superior to the most reported MOF-based electrocatalysts. Additionally, investigation of NO_3RR mechanism reveals that the structural change is favorable for the activation of $^*H_2O$ and the hydrogenation of $^*NO_3$ and $^*NO$. This work provides fundamental understanding about structural evolution of Co-MOFs during NO_3RR and guidance for the design of high-efficiency electrocatalysts.

2. Results and Discussion

ZIF-67 or Co-HHTP on CP was prepared through a one-step solvothermal method by employing cobalt nitrate hexahydrate or cobalt acetate tetrahydrate as the metal source and 2-Methylimidazole (2MZ) or 2,3,6,7,10,11-hexahydroxytriphenylene (HHTP) as the ligand, respectively.[17,18] As revealed by the scanning electron microscopy (SEM) images and digital photographs (Figure 1a, b), micrometer-sized sheet arrays are uniformly loaded on carbon fibers, which constitute the purple all-in-one electrode (ZIF-67/CP). Similarly, carbon fibers of the black binder-free electrode (Co-HHTP/CP) evenly support micrometer-long rod arrays (Figure 1c, d). The corresponding element mapping images suggest the uniform distribution of Co, C, and N elements in ZIF-67, as well as that of Co, C, and O elements in Co-HHTP (Figure 1e, f). The crystalline natures of the resultant ZIF-67 and Co-HHTP were studied by XRD patterns (Figure 1g). The low peaks at 2θ ranging from 7° to 30°correspond to the characteristic peaks of sheet-like ZIF-67.[17] And peaks at 5.1° and 9.8° are attributed to the (100) and (200) diffractions of Co-HHTP.[18] To investigate the valence state and coordination structure of ZIF-67 and Co-HHTP, X-ray absorption near-edge structure (XANES) and Fourier-transformed extended X-ray absorption fine structure (FT-EXAFS) spectra were performed.[19] As shown in the XANES spectra, the energy position of Co K-edge for ZIF-67 and Co-HHTP is close to that of CoO (Figure 1h). The result indicates that both ZIF-67 and Co-HHTP have an average valence state approaching + 2. And the slight difference in the coordination environments of ZIF-67 and Co-HHTP was further determined. In the FT-EXAFS spectra, the characteristic peak at ≈ 1.52 Å for ZIF-67 is assigned to Co-N bond; while that at ≈ 1.57 Å for Co-HHTP belongs to Co-O bond (Figure 1i).[13,20] These observations reveal that Co-MOFs with different coordination structures and the corresponding all-in-one electrodes are successfully synthesized, which are used as model catalysts for the next exploration of electrocatalytic NO_3RR.

Electrocatalytic NO_3RR performance of ZIF-67/CP and Co-HHTP/CP was evaluated in a standard three-electrode H-type cell. Firstly, the linear sweep voltammetry (LSV) curves were measured before the chronoamperometry (CA) tests in 1 M KOH electrolyte with 0.2 M KNO_3. ZIF-67/CP exhibits a greater current density at -0.8 V versus RHE than Co-HHTP/CP, while Co-HHTP/CP has a more positive onset potential relative to ZIF-67/CP (Figure 2a). Subsequently, CA tests were conducted, and the product was detected by UV-vis photometer (Figure S1). Within the wide potential range of −0.2 to −1.0 V versus RHE, both ZIF-67/CP and Co-HHTP/CP achieve NH_3 FEs greater than 95% (Figure 2b). The NH_3 yield rates of ZIF-67/CP are higher than those of Co-HHTP/CP at the overall applied potentials from -0.3 to -1.0 V versus RHE (Figure 2c). Whereas the NH_3 yield rate of Co-HHTP/CP is slightly higher than that of ZIF-67/CP at -0.2 V versus RHE, which is consistent with the result of the LSV curves. Significantly, ZIF-67/CP and Co-HHTP/CP deliver high NH_3 yield rates of 87.41 and 79.11 mg h^{-1} cm^{-2} at −1.0 V versus RHE, respectively, which are superior to the most reported MOF-based electrocatalysts (Figure 2d and Table S1). Besides, the durability of ZIF-67/CP and Co-HHTP/CP was also assessed. After consecutive NH_3 synthesis within 24 hours at -0.5 V versus RHE, negligible reduction of NH_3 FEs is observed, demonstrating the high electrochemical durability of these transformed electrodes (Figure 2e). These results demonstrate that Co-MOFs are promising electrocatalysts for nitrate reduction to ammonia.

It is worth noting that the onset potential of Co-HHTP/CP in the LSV curve after CA tests becomes more negative and remains consistent with that of ZIF-67/CP before CA tests, which is likely associated with the structural change. Hence, electrochemical impedance spectra (EIS) and electrochemical active surface area (ECSA) of these electrodes were measured before and after CA tests. As shown in Figure 2f and g, two semicircles are observed in Nyquist plots, which result from the heterogeneous charge distributions caused by two different reactions. The semicircles in the higher and lower frequency regions correspond to the reconstruction of Co-MOFs and NO_3RR, respectively.[21] The charge transfer impedances for NO_3RR gradually decrease during successive EIS tests at −0.2 V versus RHE. This manifests that the derived structure has a higher NO_3RR activity compared to ZIF-67/CP and Co-HHTP/CP. After the 15th EIS test, the impedance for the reconstruction of ZIF-67/CP becomes imperceptible, and the charge transfer impedance for NO_3RR remains nearly stable.

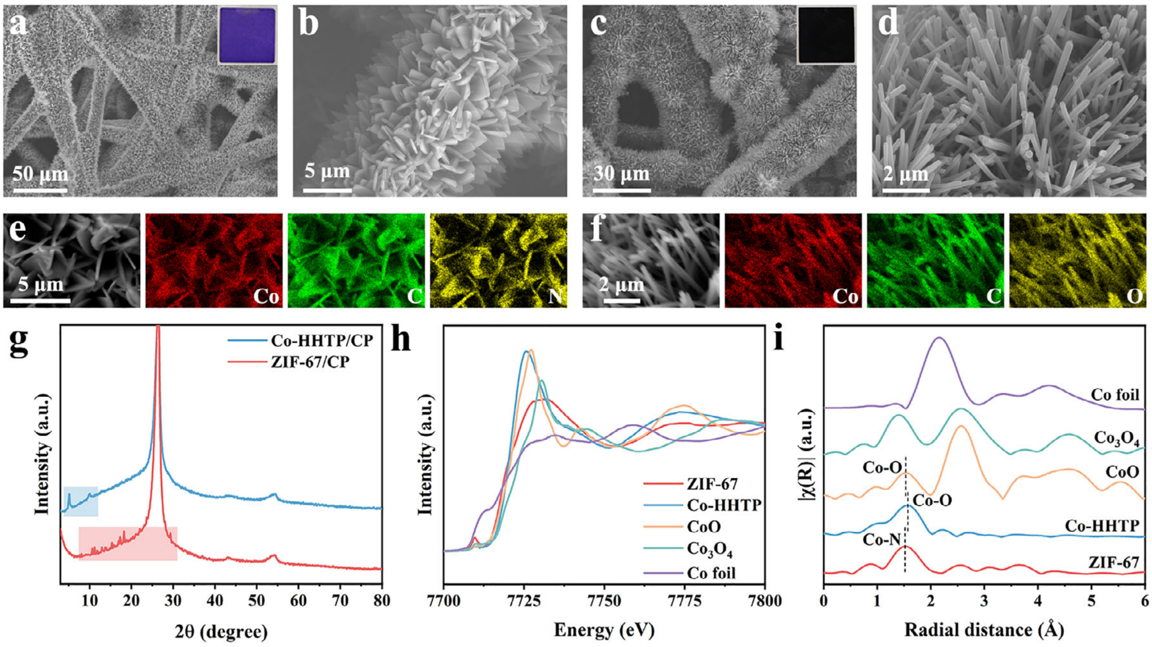

Figure 1. SEM images and digital photographs of pristine ZIF-67/CP a, b) and Co-HHTP/CP c, d). SEM and the corresponding element mapping images of pristine ZIF-67/CP e) and Co-HHTP/CP f). g) XRD patterns of pristine ZIF-67/CP and Co-HHTP/CP. Co K-edge XANES h) and FT-EXAFS i) spectra of ZIF-67, Co-HHTP and reference samples (Co foil, CoO and Co_3O_4).

But Co-HHTP/CP is different. These elucidate that ZIF-67 can achieve faster structural change than Co-HHTP during NO_3RR. Nevertheless, through prolonged CA tests and structural evolution, Co-HHTP/CP exhibits the same EIS test result as ZIF-67/CP (Figure S2). In addition to impedance, there are also significant changes of ECSA after CA tests, which is acquired by extracting the double layer capacitance (C_{dl}) from the CV curves with different scan rates (Figure S3). After CA tests, the C_{dl} of ZIF-67/CP increases markedly, while that of Co-HHTP/CP decreases markedly (Figure 2h). The slightly increased C_{dl} of ZIF-67/CP (121 mF cm^{-2}) relative to that of Co-HHTP/CP (104 mF cm^{-2}) suggests that ZIF-67/CP has the larger ECSA and better electrochemical performance than Co-HHTP/CP. These above differences before and after CA tests prove the existence of reconstruction.

Furthermore, the structural characterizations after the reaction were performed. As shown in XRD patterns, the characteristic peaks of ZIF-67 after LSV test disappear (Figure 3a). While peaks at 19.1°, 32.6°, 38.0°, and 51.5° are observed, which correspond to (001), (100), (011), and (012) facets of $Co(OH)_2$, respectively. Even after long-term CA tests, the characteristic peaks of $Co(OH)_2$ still exist (Figure S4). SEM and TEM images uncover that the micrometer-sized sheets of ZIF-67/CP are reconstructed into nanosheets (Figures 3b and S5). The high-resolution TEM (HRTEM) image and the corresponding fast Fourier transform (FFT) pattern further confirm the formation of $Co(OH)_2$ (Figure 3c). Moreover, X-ray photoelectron spectroscopy (XPS) analysis shows that peaks at 781.42 and 797.12 eV in Co *2p* spectrum of pristine ZIF-67/CP are assigned to Co^{2+} $2p_{3/2}$ and Co^{2+} $2p_{1/2}$, respectively (Figure 3d). This elucidates that Co of the synthesized ZIF-67 has a valence state of + 2 and a uniform coordination environment, which is in accordance with the result of the XANES and FT-EXAFS. For ZIF-67/CP after LSV or CA tests, signals in Co *2p* spectrum include Co^{3+} $2p_{3/2}$, Co^{2+} $2p_{3/2}$, Co^{3+} $2p_{1/2}$, and Co^{2+} $2p_{1/2}$, which belong to $Co(OH)_2$ after NO_3RR in alkaline electrolyte solution (Figures 3d and S6a).[22] And N signals in the N *1s* spectrum and the element mapping image of ZIF-67 after LSV or CA tests are all negligible, which attests to the complete removal of the organic ligands (Figures 3e, f and S6b). Whereafter, CV curves were measured to obtain the surface concentration of active Co centers, which was extracted from the linear relationship between the scan rates and the peak current densities of the Co^{3+}/Co^{2+} reduction wave (Figure S7a, b).[23] The surface concentrations of electrochemical active Co centers over ZIF-67/CP before and after CA tests are 189 and 97 nmol cm^{-2}, respectively (Figure S7e). The loss is caused by the size variation of sheet-like ZIF-67 and $Co(OH)_2$. All the above validate that the Co-N coordinated ZIF-67 can be easily reconstructed into $Co(OH)_2$ nanosheets during LSV test, and this $Co(OH)_2$ structure remains unchanged after the subsequent CA tests.

Similarly, the characteristic peaks in XRD patterns of pristine Co-HHTP/CP sample also disappear after LSV test. Differently, no $Co(OH)_2$ signal is detected (Figure 3a). And there is no obvious difference in the Co *2p* spectra of Co-HHTP/CP before and after LSV test, which unravels that the Co-HHTP after LSV test is still linked by metal ions and oxygen organic ligands (Figure S8). Nevertheless, Co-HHTP was reconstructed into $Co(OH)_2$ during CA tests (Figure 3a, g and i). The $Co(OH)_2$ derived from Co-HHTP has the micrometer-sized sheet-like morphology (Figures 3h and S9). These results clarify that the Co-O coordinated Co-HHTP has the lower structure evolution rate than ZIF-67 during the nitrate reduction process, which requires a longer time for complete reconstruction of Co-HHTP into $Co(OH)_2$. Such obvious morphological change leads to a greater loss of surface active Co center concentration, which decreases from 306 to 77 nmol cm^{-2}

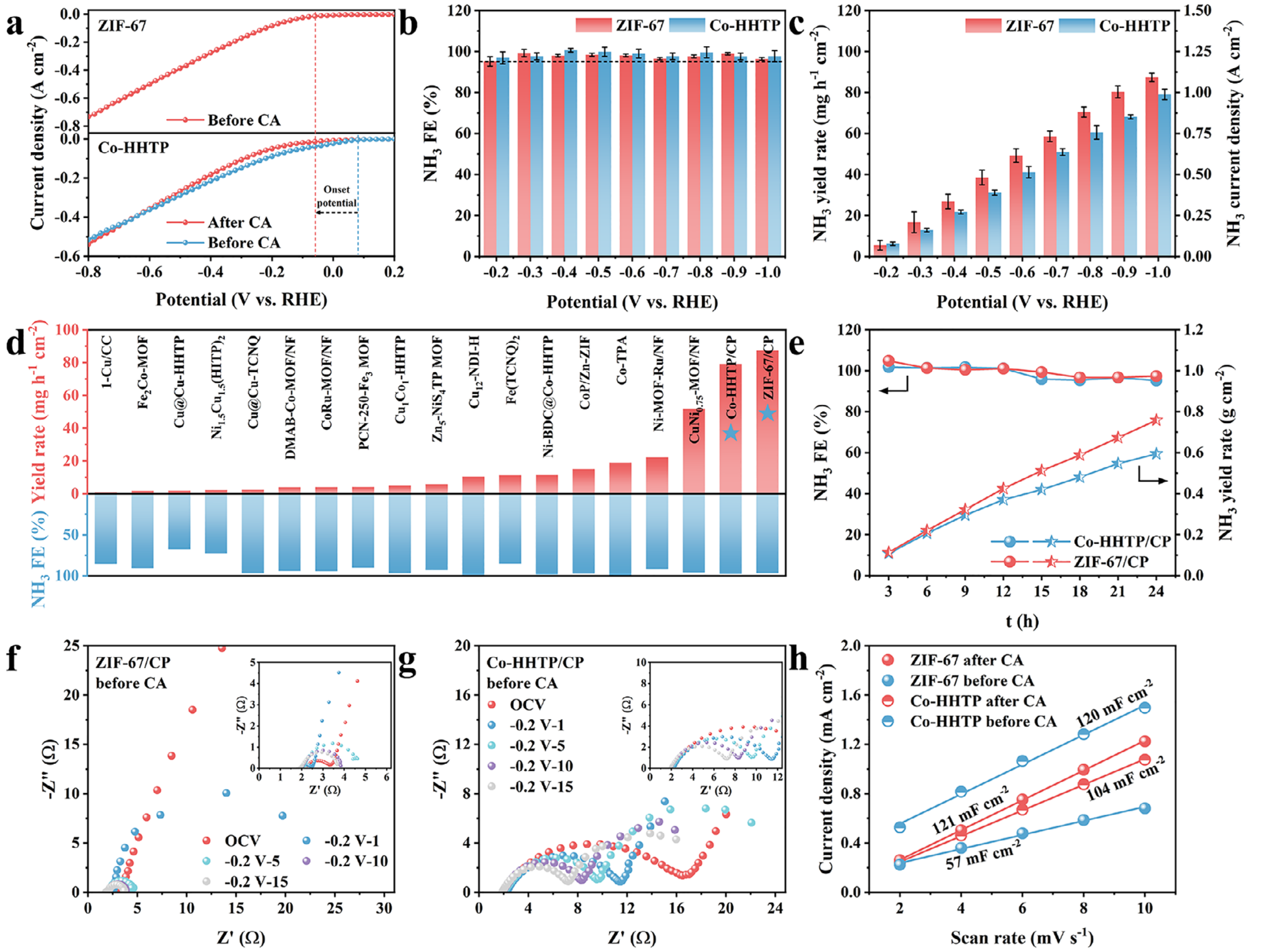

Figure 2. a) LSV curves of ZIF-67/CP and Co-HHTP/CP before or after CA tests in 1 M KOH electrolyte with 0.2 M KNO_3. NH_3 FEs b) and yield rates c) of ZIF-67/CP and Co-HHTP/CP at different potentials. d) Performance comparison with reported MOF-based electrocatalysts. e) Consecutive NH_3 synthesis over ZIF-67/CP and Co-HHTP/CP within 24 hours at -0.5 V versus RHE. Nyquist plots obtained from successive multiple EIS tests of pristine ZIF-67/CP f) and Co-HHTP/CP g) at the OCV and −0.2 V versus RHE. h) Plots of capacitive current density versus the scan rate over ZIF-67/CP and Co-HHTP/CP before or after CA test.

(Figure S7c, d, and f). The resultant turnover frequency (TOF) of ZIF-67/CP after reconstruction is slightly greater than that of Co-HHTP/CP (Figure S10). The lower surface Co concentration and TOF of Co-HHTP/CP relative to those of ZIF-67/CP also account for the slightly lower NH_3 yield rates of Co-HHTP/CP.

Moreover, the catalytic performance of commercial $Co(OH)_2$, pure HHTP and bare CP were also investigated. Within the wide potential range of −0.2 to −1.0 V versus RHE, $Co(OH)_2$/CP achieves similar NH_3 FEs greater than 90% (Figure S11). The NH_3 yield rates are slightly less than those of all-in-one ZIF-67/CP and Co-HHTP/CP at overall applied potentials, which highlights the advantages of the free-standing electrode over effective electron transfer. After CA tests, its crystalline structure and morphology remain unchanged (Figure S12). Besides, the current density, NH_3 yield rate and FE of HHTP on CP and bare CP are much lower than those of $Co(OH)_2$/CP (Figure S13). These results indicate that the residual HHTP during the early stage of NO_3RR have the negligible promoting effect in NO_3RR. And $Co(OH)_2$ is the real catalytic species.

To further shed light on the structural evolution of ZIF-67/CP and Co-HHTP/CP, in-situ Raman spectra were recorded under different times and potentials. Firstly, the characteristic Raman modes of ZIF-67 were measured under the open-circuit voltage (OCV). The modes at shifts of 258, 315, 425, 501, 687, 1146, 1180, 1457, and 1499 cm^{-1} are assigned to ZIF-67 (Figure 4a). Subsequently, a potential of −0.2 V versus RHE was applied to the electrode for NO_3RR. The intensities of peaks at 258, 315, 425, 1146, 1180, 1457, and 1499 cm^{-1} gradually decrease and eventually these peaks completely disappear after 5 minutes. Among them, the detail of the mode at 425 cm^{-1} is presented in Figure 4b and c. This establishes that the organic ligands of ZIF-67 can be easily removed even at a low potential. Moreover, the intensity of the peak at 501 cm^{-1} first weakens and then increases. The latter corresponds to the emergence of the A_{2u} mode about $Co(OH)_2$.[24] Meanwhile, a peak appears at 480 cm^{-1} after the application of potentials and intensifies along with the peak at 687 cm^{-1}. They separately belong to the E_g and A_{1g} modes of Co_3O_4, which likely come from the inevitable phase transition

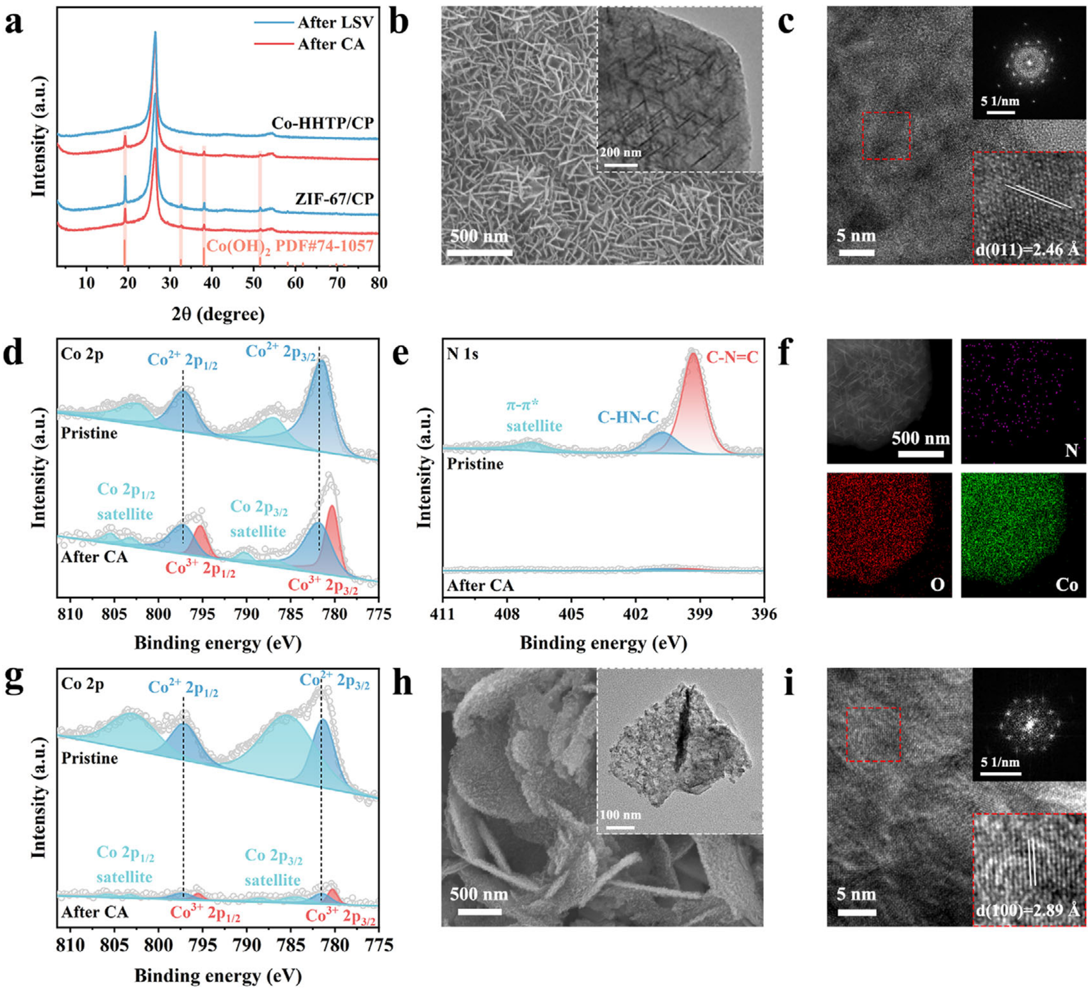

Figure 3. a) XRD patterns of ZIF-67/CP and Co-HHTP/CP after LSV or CA test. SEM b), TEM (insert of b), HRTEM c) images and the corresponding FFT pattern (insert of c) of ZIF-67/CP after CA test. XPS spectra of Co *2p* d) and N *1s* e) over ZIF-67/CP after CA tests or pristine ZIF-67/CP. f) HAADF-STEM and the corresponding element mapping images of ZIF-67/CP after CA test. g) Co *2p* XPS spectra of Co-HHTP/CP after CA test or pristine Co-HHTP/CP. SEM h), TEM (insert of h), HRTEM i) images and the corresponding FFT pattern (insert of i) of Co-HHTP/CP after CA test.

from $Co(OH)_2$ to Co_3O_4 triggered by laser oxidation.[25,26] And no Co_3O_4 is observed by XRD and TEM. These observations further corroborate the in-situ structural evolution of ZIF-67 to $Co(OH)_2$, which is the real active site of NO_3RR over ZIF-67. Besides, the in-situ Raman modes of Co-HHTP are shown in Figure 4d and e. However, with the application of multiple potentials and the extension of test time, the characteristic modes (697 cm^{-1}, 1380–1550 cm^{-1}) of Co-HHTP remain unchanged. And the modes of $Co(OH)_2$ are not detected, which clearly certifies the higher coordination environment stability of Co-HHTP. After in-situ Raman test, the same electrode was used for XRD characterization (Figure 4f). $Co(OH)_2$ is only found in the sample ZIF-67/CP after in-situ Raman test.

To uncover the influence of structural evolution on NO_3RR, in-situ Bode analysis was used to track the electrochemical process of NO_3RR. Similar to the Nyquist plots, peaks in the high frequency region are related to the reconstruction of Co-MOFs, while peaks in the low frequency region are related to the adsorption of $^*NO_3$ and $^*H$ (Figure 5a, b).[27] For ZIF-67/CP, the phase angle in the high frequency region decreases and approaches 0° during successive EIS tests at -0.2 V versus RHE, which corresponds to the fast reconstruction. The phase angle in the low frequency region reduces synchronously, and the peak position shifts to a higher frequency. This unravels that the structural change enhances the adsorption of $^*NO_3$ and $^*H$, thereby facilitating NO_3RR.[28] For Co-HHTP/CP, the phase angles and positions of the peaks in both the high and low frequency regions hardly change anymore after the 15th EIS test at -0.2 V versus RHE. Nonetheless, after CA tests, the response of Co-HHTP reconstruction disappears, and the response of NO_3RR over Co-HHTP becomes the same as that over ZIF-67 (Figure 5c). These clarify that $Co(OH)_2$, as the active phase, has stronger adsorption of adsorbates and faster charge transfer of NO_3RR than ZIF-67 and Co-HHTP. Subsequently, Co-N bond of ZIF-67 was proved to have a longer bond length and a smaller bond energy (1.92 Å and 2.33 eV) relative to Co-O bond of Co-HHTP (1.83 Å and 2.81 eV), which would lead to the faster transformation of ZIF-67 into $Co(OH)_2$ (Figures S14 and S15, and Table S2).

In addition, the reaction pathway of NO_3RR over ZIF-67 and Co-HHTP was studied through identifying the reaction

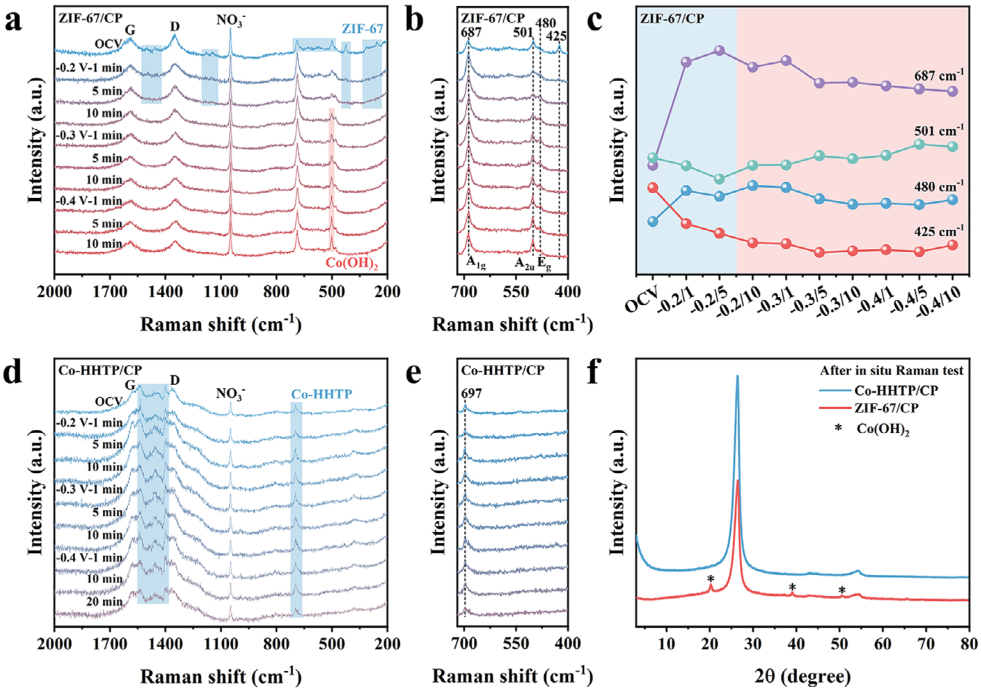

Figure 4. a, b) Electrochemical in-situ Raman spectra of ZIF-67/CP. c) Intensity variation graph of the Raman modes over ZIF-67/CP. d, e) Electrochemical in-situ Raman spectra of Co-HHTP/CP. f) XRD patterns of ZIF-67/CP and Co-HHTP/CP after in-situ Raman test.

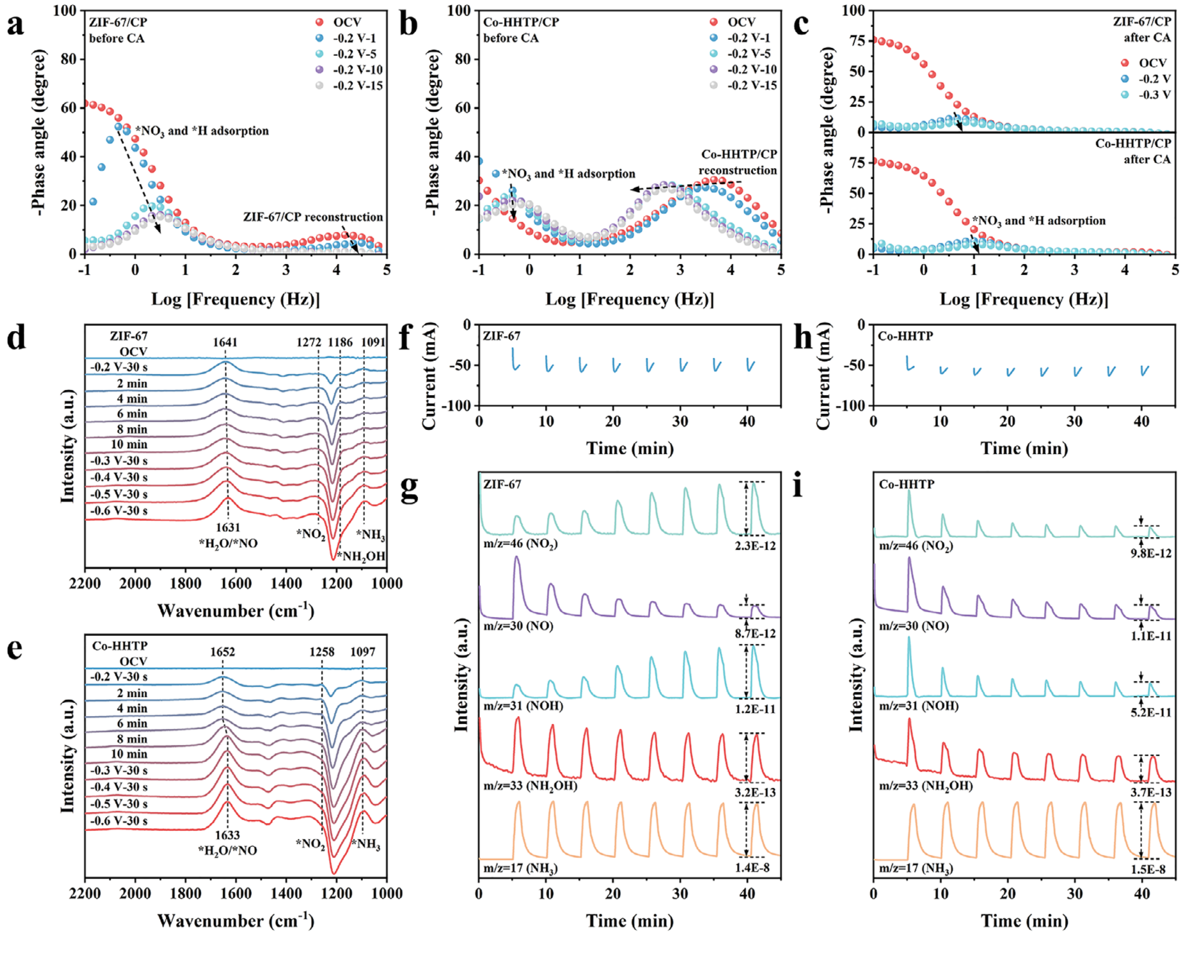

Figure 5. Bode phase plots obtained from successive multiple EIS tests of pristine ZIF-67/CP a) and Co-HHTP/CP b) at the OCV and -0.2 V versus RHE. c) Bode phase plots of ZIF-67/CP and Co-HHTP/CP at different potentials after CA tests. Electrochemical in-situ FTIR spectra of ZIF-67/CP d) and Co-HHTP/CP e). I-t curves of intermittent CA tests at -0.3 V versus RHE and the corresponding DEMS analysis over ZIF-67/CP f, g) and Co-HHTP/CP h, i).

intermediates using in-situ Fourier transform infrared (FTIR) and differential electrochemical mass spectroscopy (DEMS). Considering the reconstruction of ZIF-67, a time-dependent test at −0.2 V versus RHE was performed, and then the potential increased sequentially (Figure 5d). The spectra bands at 1091 and 1186 cm^{-1} correspond to the stretching vibration mode of N-H bond in $*NH_3$ and $*NH_2OH$, respectively.[29] The adsorption band at 1272 cm^{-1} is attributed to the symmetric and antisymmetric stretching vibration of $*NO_2$.[30] And the characteristic band at 1641 cm^{-1} is assigned to the bending vibration of the adsorbed water ($*H_2O$) and the vibration mode of *NO.[31,32] As time and potential increase, the peak of $*H_2O$ shifts to low wavenumbers continuously and its intensity increases, which stems from the transformation of ZIF-67 to $Co(OH)_2$. At the same time, the signal intensity of $*NH_2OH$ weakens, while those of $*NO_2$ and $*NH_3$ enhance. These elucidate that the structural change promotes the activation and cracking of $*H_2O$, which contributes to the hydrogenation of $*NO_3$ and $*NH_2OH$ as well as the generation of $*NH_3$.[33,34] For Co-HHTP, the position of $*H_2O$ only shifts toward the low wavenumbers in the 6th to 10th min of the test, and remains constant before and after this period (Figure 5e). Such a result is caused by the stable Co-O coordination environment and the partial reconstruction of Co-HHTP.

DEMS was also measured during the intermittent CA tests at -0.3 V versus RHE. Under test conditions, ZIF-67 exhibits a current of around 50 mA (Figure 5f). And the DEMS analysis of ZIF-67 records the mass-to-charge (m/z) signals of 46, 30, 31, 33, and 17, which correspond to NO_2, NO, NOH, NH_2OH, and NH_3, respectively (Figure 5g). Along with the generation of $Co(OH)_2$, the signal intensities of NO_2 and NOH increase, while that of NO decreases, which further evidences the more favorable hydrogenation of NO_3 and NO promoted by the structural evolution. Unlike ZIF-67, the contents of NO_2, NO, NOH, and NH_2OH intermediates over Co-HHTP all decrease and eventually become constant (Figure 5 h, i). Meanwhile, under nearly the same current response, the amounts of NO_2, NO, and NOH over Co-HHTP are much higher than those over ZIF-67. These all are on account of incomplete structural transformation and the slower hydrogenation rate of Co-HHTP, which agrees with its lower NH_3 yield rate.

3. Conclusion

In conclusion, all-in-one Co-MOF electrodes with different coordinated environments have been constructed for promoting electrocatalytic NO_3RR, wherein insightful understanding of in-situ structural evolution was obtained. As revealed by various in-situ and ex-situ characterizations, both Co-N coordinated ZIF-67 and Co-O coordinated Co-HHTP would be transformed into $Co(OH)_2$, which is recognized as the real active site for NO_3RR. Benefiting from this structural transformation, the more favorable activation of $*H_2O$ and hydrogenation of $*NO_3$ and *NO are realized, leading to the wide-potential and high-yield electrochemical NH_3 synthesis. Our work demonstrates the significant role of structural evolution in promoting catalytic performance, and also provides the guidance for developing efficient MOF-based electrocatalysts.

Supporting Information

The authors have cited additional references within the Supporting Information.[13,35–50]

Acknowledgments

This work was supported by National Key R&D Program of China (2021YFB4000402), the National Natural Science Foundation of China (52273277), Jilin Province Science and Technology Development Plan Funding Project (SKL202302039) and Youth Innovation Promotion Association CAS (2021223). H.X.Z. acknowledges funding from National Natural Science Foundation of China Outstanding Youth Science Foundation of China (Overseas). These authors also thank Prof. Junmin Yan, Zhe Meng and Xuefeng Sun from Jilin University for in-situ Raman and DEMS measurements and analysis.

Conflict of Interest

The authors declare no conflict of interest.

Data Availability Statement

The data that support the findings of this study are available from the corresponding author upon reasonable request.

Keywords: ammonia production • cobalt-based metal-organic frameworks • electrocatalysis • nitrate electroreduction • structural evolution

[1] J. G. Chen, R. M. Crooks, L. C. Seefeldt, K. L. Bren, R. M. Bullock, M. Y. Darensbourg, P. L. Holland, B. Hoffman, M. J. Janik, A. K. Jones, M. G. Kanatzidis, P. King, K. M. Lancaster, S. V. Lymar, P. Pfromm, W. F. Schneider, R. R. Schrock, *Science* **2018**, *360*, eaar6611.
[2] L. Zhai, S. Liu, Z. Xiang, *Ind. Chem. Mater.* **2023**, *1*, 332.
[3] Y. Zhang, J. Li, Y. Zhou, C.-t. Au, X. Wang, L. Jiang, *Fundam. Res.* **2024**, *11*, 016.
[4] V. T. Chebrolu, D. Jang, G. M. Rani, C. Lim, K. Yong, W. B. Kim, *Carbon Energy* **2023**, *5*, e361.
[5] T. Wu, Y. Du, Z. J. Zuo, S. Li, J. Wu, J. Gao, T. Mu, Y. C. Zhang, X. D. Zhu, *Adv. Funct. Mater.* **2025**, 2424142.
[6] G. Huang, H. Liu, Y. Li, J. Zhu, Y. Ge, C. Liu, Q. Tian, B. Gao, Y. Liu, B. Han, Q. Xu, *Adv. Funct. Mater.* **2025**, 2500577.
[7] Z. Wang, F. Zhou, B. Lv, J. Yu, J. Zhang, Y. Zhang, Y. Wu, Y. Wang, W. Luo, *Adv. Sustainable Syst.* **2025**, e00211.
[8] L. Xiao, S. Mou, X. Lin, K. Wu, S. Liu, W. Dai, W. Yang, C. Tang, C. Long, F. Dong, *Green Energy Environ.* **2025**, *03*, 009.
[9] R. Cao, S. Yin, Y. Han, J. Zhang, W. Jiang, G. Liu, *Coord. Chem. Rev.* **2025**, *538*, 216722.
[10] T. H. Dolla, B. Zhang, T. Matthews, M. P. Chabalala, S. O. Ajayi, L. L. Sikeyi, X. Liu, M. K. Mathe, *Coord. Chem. Rev.* **2024**, *518*, 216061.
[11] C. Wang, Z. Lv, Y. Liu, L. Dai, R. Liu, C. Sun, W. Liu, X. Feng, W. Yang, B. Wang, *Angew. Chem., Int. Ed.* **2024**, *63*, e202411216.
[12] X. Zhao, S. Wang, Y. Cao, Y. Li, A. S. Portniagin, B. Tang, Q. Liu, P. Kasák, T. Zhao, X. Zheng, Y. Deng, A. L. Rogach, *Adv. Sci.* **2024**, *11*, 2405936.
[13] Y. Zou, Y. Yan, Q. Xue, C. Zhang, T. Bao, X. Zhang, L. Yuan, S. Qiao, L. Song, J. Zou, C. Yu, C. Liu, *Angew. Chem., Int. Ed.* **2024**, *63*, e202409799.
[14] Y. Xu, Q. Li, H. Xue, H. Pang, *Coord. Chem. Rev.* **2018**, *376*, 292.

[15] Q. Qi, C. Zhang, J. Hu, *Coord. Chem. Rev.* **2025**, *522*, 216235.

[16] J. Yang, H. Qi, A. Li, X. Liu, X. Yang, S. Zhang, Q. Zhao, Q. Jiang, Y. Su, L. Zhang, J.-F. Li, Z.-Q. Tian, W. Liu, A. Wang, T. Zhang, *J. Am. Chem. Soc.* **2022**, *144*, 12062.

[17] S. Li, L. Sun, H. Gao, Y. Long, S. Guo, Q. Jia, Y. Jiang, Z. Ye, *Chem. Eng. J.* **2025**, *512*, 162370.

[18] Y. He, F. Yan, X. Zhang, C. Zhu, Y. Zhao, B. Geng, S. Chou, Y. Xie, Y. Chen, *Adv. Energy Mater.* **2023**, *13*, 2204177.

[19] B. Ravel, M. Newville, ATHENA, A., *J. Synchrotron Radiat.* **2005**, *12*, 537.

[20] T. Kuang, L. Deng, M. Liu, Y. Ding, W. Guo, Z. Cai, W. Liu, Z. X. Huang, *Adv. Mater.* **2025**, 2415616.

[21] Y. Qi, Y. Zhang, L. Yang, Y. Zhao, Y. Zhu, H. Jiang, C. Li, *Nat. Commun.* **2022**, *13*, 4602.

[22] D. X. Liu, Z. Meng, Y. F. Zhu, X. F. Sun, X. Deng, M. M. Shi, Q. Hao, X. Kang, T. Y. Dai, H. X. Zhong, J. M. Yan, Q. Jiang, *Angew. Chem., Int. Ed.* **2023**, *63*, e202315238.

[23] J. Wang, K. Li, H. x. Zhong, D. Xu, Z. l. Wang, Z. Jiang, Z. j. Wu, X. b. Zhang, *Angew. Chem., Int. Ed.* **2015**, *54*, 10530.

[24] L. Qiao, A. Zhu, D. Liu, K. An, J. Feng, C. Liu, K. W. Ng, H. Pan, *Adv. Energy Mater.* **2024**, *14*, 2402805.

[25] P. Gao, Y. Zeng, P. Tang, Z. Wang, J. Yang, A. Hu, J. Liu, *Adv. Funct. Mater.* **2021**, *32*, 2108644.

[26] W. Zheng, M. Liu, L. Y. S. Lee, *ACS Catal.* **2019**, *10*, 81.

[27] S. Luo, H. Guo, T. Li, H. Wu, F. Zhang, C. Tang, G. Chen, G. Yang, Y. Zhou, *Appl. Catal. B* **2024**, *351*, 123967.

[28] J. H. Dong, X. Z. Song, Y. X. Chen, Z. X. Gai, Z. Yuan, D. K. Liu, Z. Tan, A. Liu, X. F. Wang, S. Y. Song, *Adv. Funct. Mater.* **2025**, 2422025.

[29] R. Zhang, C. Li, H. Cui, Y. Wang, S. Zhang, P. Li, Y. Hou, Y. Guo, G. Liang, Z. Huang, C. Peng, C. Zhi, *Nat. Commun.* **2023**, *14*, 8036.

[30] B. Lv, J. Yu, F. Zhou, Z. Wang, J. Zhang, Y. Zhang, Y. Wu, Y. Wang, W. Luo, *Mol. Catal.* **2025**, *578*, 114978.

[31] X. Chen, Y. Cheng, B. Zhang, J. Zhou, S. He, *Nat. Commun.* **2024**, *15*, 6278.

[32] A. Huang, J. Yu, J. Zhang, Y. Zhang, Y. Wu, Y. Wang, W. Luo, *Catalysts* **2025**, *15*, 199.

[33] F. Tian, S. Geng, M. Li, L. Qiu, F. Wu, L. He, J. Sheng, X. Zhou, Z. Chen, M. Luo, H. Liu, Y. Yu, W. Yang, S. Guo, *Adv. Mater.* **2025**, *37*, 2501230.

[34] J. Yu, Z. Xi, J. Su, P. Jing, X. Xu, B. Liu, Y. Wang, J. Zhang, *eScience* **2025**, *5*, 100350.

[35] C. Yang, Y. Tang, Q. Yang, B. Wang, X. Liu, Y. Li, W. Yang, K. Zhao, G. Wang, Z. Wang, F. Yu, *J. Hazard. Mater.* **2024**, *480*, 136036.

[36] Y. Yao, X. Wei, H. Zhou, K. Wei, B. Kui, F. Wu, L. Chen, W. Wang, F. Dai, P. Gao, N. Wang, W. Ye, *ACS Catal.* **2024**, *14*, 16205.

[37] J. Yang, W.-D. Zhang, H. Zhao, Y. Zou, Z.-Y. Zhang, J. Liu, J. Wang, Z.-G. Gu, X. Yan, *Appl. Catal. B* **2024**, *340*, 123237.

[38] C. Zhang, Y. Zhang, R. Deng, L. Yuan, Y. Zou, T. Bao, X. Zhang, G. Wei, C. Yu, C. Liu, *Adv. Mater.* **2024**, *36*, 2313844.

[39] N. Mukherjee, A. Adalder, N. Barman, R. Thapa, R. Urkude, B. Ghosh, U. K. Ghorai, *J. Mater. Chem. A* **2024**, *12*, 3352.

[40] Q. Li, L. Luo, X. Guo, R. Wang, J. Liu, W. Fan, Z. Feng, F. Zhang, *J. Am. Chem. Soc.* **2024**, *147*, 1884.

[41] Z. Zhang, Y. Lv, Y. Gu, X. Zhou, B. Tian, A. Zhang, Z. Yang, S. Chen, J. Ma, M. Ding, J. L. Zuo, *Angew. Chem., Int. Ed.* **2024**, *64*, e202418272.

[42] P. Liu, J. Yan, H. Huang, W. Song, *Chem. Eng. J.* **2023**, *466*, 143134.

[43] A. K. K. Padinjareveetil, J. V. Perales-Rondon, D. Zaoralová, M. Otyepka, O. Alduhaish, M. Pumera, *ACS Appl. Mater. Interfaces* **2023**, *15*, 47294.

[44] T. Ren, Z. Yu, H. Yu, K. Deng, Z. Wang, X. Li, H. Wang, L. Wang, Y. Xu, *ACS Nano* **2023**, *17*, 12422.

[45] T. Ren, H. Wang, S. Xu, H. Yu, K. Deng, Z. Wang, H. Wang, L. Wang, Y. Xu, *J. Mater. Chem. A* **2023**, *11*, 24854.

[46] N. Zhou, J. Wang, N. Zhang, Z. Wang, H. Wang, G. Huang, D. Bao, H. Zhong, X. Zhang, *Chin. J. Catal.* **2023**, *50*, 324.

[47] J. Yan, J. Li, P. Liu, H. Huang, W. Song, *Green Chem.* **2023**, *25*, 8645.

[48] X. Zhu, H. Huang, H. Zhang, Y. Zhang, P. Shi, K. Qu, S.-B. Cheng, A.-L. Wang, Q. Lu, *ACS Appl. Mater. Interfaces* **2022**, *14*, 32176.

[49] Y. Lv, S. W. Ke, Y. Gu, B. Tian, L. Tang, P. Ran, Y. Zhao, J. Ma, J. L. Zuo, M. Ding, *Angew. Chem., Int. Ed.* **2023**, *62*, e202305246.

[50] Y.-T. Xu, M.-Y. Xie, H. Zhong, Y. Cao, *ACS Catal.* **2022**, *12*, 8698.

Manuscript received: May 23, 2025
Revised manuscript received: June 23, 2025
Version of record online: July 11, 2025